Check for updates

# Colloidal synthesis of a heterostructured CuCo₂S₄/g-C₃N₄/In₂S₃ nanocomposite for photocatalytic hydrogen evolution†

Amit Gautam,[ab] Saddam Sk, [ID][ab] Aparna Jamma,[ab] B Moses Abraham,[c] Mohsen Ahmadipour[d] and Ujjwal Pal [ID] *[ab]

The introduction of the hot injection approach in designing effective nanocomposites with hetero-structures significantly enhances the photocatalytic performance by reinforcing their active sites and facilitating the directed transfer of photocarriers. Here, we present a rapid and easy fabrication process for the synthesis of $CuCo_2S_4$ and $CuCo_2S_4$/g-$C_3N_4$/$In_2S_3$ heterostructures by the colloidal hot injection method and employed them for photocatalytic $H_2$ generation under visible light irradiation. The as-prepared materials exhibit unique properties, specifically visible light absorption, suppressed re-combination of photogenerated charge carriers, and sustainable $H_2$ production over prolonged exposure to light irradiation. The catalysts were characterized well to investigate the structural, photophysical and electronic properties. In the $CuCo_2S_4$/g-$C_3N_4$/$In_2S_3$ composite, $CuCo_2S_4$ and $In_2S_3$ nanoparticles are deposited on 2D g-$C_3N_4$. The post synthetically modified hybrid photocatalyst $CuCo_2S_4$/g-$C_3N_4$/$In_2S_3$ greatly influences the redox and $e^-$–$h^+$ separation process and exhibits an impressive rate of HER ($\sim$11.66 mmol $h^{-1}g^{-1}$), suppressing the pristine $CuCo_2S_4$ ($\sim$1.32 mmol $h^{-1}g^{-1}$). Because of the band gap energy and potential of the conduction band of the components, we proposed a type-I scheme of photocatalytic reaction. The experimental results indicate that the heterostructured materials exhibit remarkably high activity for hydrogen evolution. The DFT results demonstrate the role of g-$C_3N_4$ and $In_2S_3$ in improving the photocatalytic performance of the hybrid $CuCo_2S_4$ catalyst, which leads to superior catalytic behaviour. Furthermore, the increased photocatalytic activity of $CuCo_2S_4$/g-$C_3N_4$/$In_2S_3$ is ascribed to the synergistic interaction of $CuCo_2S_4$, $In_2S_3$ nanoparticles and g-$C_3N_4$, which form an electron transfer channel to harvest photo-generated electrons.

## Introduction

Solar energy is an inexhaustible, green, and renewable energy source on Earth. According to estimations, the Earth receives $1.73 \times 10^5$ TW per hour energy in the form of light, which exceeds the worldwide energy consumption throughout the year.[1,2] However, the intermittent nature of sunlight is a major obstacle to effective utilization of solar light. Hence, the storage of solar irradiation in the form of chemical fuel will be a promising approach to meet the energy needs in the future

and remediation of environmental damage because of extensive use of fossil fuels.[3–5] Hydrogen is amongst the most suitable fuels owing to its high calorific value, zero carbon emissions and non-hazardous combustion product.[6–8] Solar driven water splitting to produce hydrogen by using semiconductor photocatalysts has attracted immense research interest.[9–12] The first report of photo induced hydrogen evolution on a semiconductor photocatalyst was reported by Fujishima and Honda in 1972. They reported photo-electrochemical water splitting and utilized platinised $TiO_2$ as a photoanode.[13] After that, several photocatalysts have been synthesised for photocatalytic hydrogen evolution from water. Photocatalytic water splitting reaction involves two half reactions: photo oxidation of $H_2O$ and reduction of $H^+$.[11]

$$H_2O + h_{vb}^+ \rightarrow 2H^+ + \frac{1}{2}O_2 \,(\text{Photo oxidation of } H_2O) \quad (1)$$

$$2H^+ + 2e_{cb}^- \rightarrow H_2 \,(\text{Photo reduction of } H^+) \quad (2)$$

[a] Department of Energy & Environmental Engineering, CSIR-Indian Institute of Chemical Technology, Hyderabad-500007, India. E-mail: upal03@gmail.com, ujjwalpal@iict.res.in

[b] Academy of Scientific and Innovative Research (AcSIR), Ghaziabad-201002, India

[c] Department of Chemical Engineering, Indian Institute of Technology Kanpur, Kanpur-208016, India

[d] Institute of Microengineering and Nanoelectronics, Universiti Kebangsaan Malaysia, 43600 Bangi, Selangor, Malaysia

† Electronic supplementary information (ESI) available. See DOI: https://doi.org/10.1039/d3ya00191a

An ideal photocatalyst should have some essential properties for overall water splitting. The energy difference between the conduction band (CB) and valence band (VB) should be $>1.23$ eV. Furthermore, the CB should be more negative than redox couple $H^+/H_2$ *vs.* RHE,[14] while the VB should be more positive than $O_2/H_2O$ *vs.* RHE. $TiO_2$ is a widely studied photocatalyst for hydrogen evolution. It is an environmentally friendly, stable photocatalyst and the position of the CB and VB is well suited for overall water splitting. However, the large energy difference between the CB and VB of $TiO_2$ ($>3$ eV) enables the utilization of UV-light, which contributes $<5\%$ of solar irradiation, and the high rate of charge carrier recombination restricts the practical use of $TiO_2$ for hydrogen evolution.[15,16] The development of photocatalysts with narrow bands has become essential to utilize the visible region of the solar spectrum, since the solar spectrum consists of 40% visible light. After that various binary ($CdS$,[17] $In_2S_3$,[18] $CoS$,[19] *etc.*), composite ($ZnCdS$–$rGO/MoS_2$,[20] $MoS_2/ZnCdS/ZnS$,[21] $ZnS/ZnO/MoS_2$,[22] $Cu/BN@PANI$,[23] $Cu(OH)_2/P(C_3N_4)/MoS_2$[24] *etc.*) and quantum dot ($MoS_2$,[25] $CdS/rGO$,[26] *etc.*) photocatalyst materials were designed for photocatalytic water splitting. Transition metal sulphides are superior light harvesting materials compared to their oxide counterparts. In general, the amount of photon absorption determines the photocatalytic activity. Photocatalysts with high absorption show enhanced catalytic activity.[11] Furthermore, $CdS/CuCo_2S_4$[17] and $TiO_2/MoS_2$[15] are such examples of promising photocatalysts, exhibiting excellent photoelectrical properties for hydrogen evolution. Transition metal dichalcogenides are extensively applied for solar water splitting experiments on account of their layered structure and highly active edge sites.[11] In recent years, ternary transition metal sulphides have emerged as potential materials for photocatalytic application. Numerous ternary transition metal sulphides ($CdIn_2S_4$,[27] $ZnIn_2S_4$,[28,29] $CuCo_2S_4$,[17] and $CaIn_2S_2$[30]) with the $AB_2X_4$ composition could be potential photocatalysts for solar water splitting owing to their considerable chemical stability and optical band gap. Only a few examples are found for photocatalytic hydrogen evolution application of $CuCo_2S_4$. Furthermore, morphology, size and composition greatly influence the photocatalytic activity of materials. The major drawbacks of photocatalytic water splitting are the slow diffusion of charge carriers, and high rate of recombination.[3] Separation of photo-induced electrons and holes is challenging. The design of heterostructures is an effective way to separate the photogenerated electron hole pairs, effectively. The noble metals (Au, Pt, Ru *etc.*) have been employed as effective co-catalysts for the separation of photogenerated charge carriers.[31] The metal nanoparticles usually act as an electron sink and the holes are consumed by sacrificial electron donors. However, the limited abundance and high cost restrict the use of noble metals for practical application of water splitting. Therefore, it is indispensable to design efficient and cost-effective co-catalysts.

Two dimensional (2-D) materials such as $g$-$C_3N_4$ with a large surface to volume ratio, high stability and excellent photoelectrochemical properties have attracted much attention in photo-catalysis applications.[32,33] $g$-$C_3N_4$ has an optical band gap of 2.7 eV, which falls in the visible region of the solar spectrum. In addition, the potential of CB and VB is well suited for redox reaction of water.[24,34,35]

In this work, we have designed $CuCo_2S_4/g$-$C_3N_4/In_2S_3$ by the hot injection method. The obtained photocatalyst shows excellent activity for hydrogen evolution, which was much higher than that of $CuCo_2S_4$, $CuCo_2S_4/g$-$C_3N_4$, $CuCo_2S_4/In_2S_3$ and $In_2S_3/g$-$C_3N_4$. In this strategy, $CuCo_2S_4$ and $In_2S_3$ nanoparticles are evenly dispersed on $g$-$C_3N_4$ and show good crystallinity and well-defined morphology. The UV-visible absorption analysis indicates enhanced light absorption by $CuCo_2S_4/g$-$C_3N_4/In_2S_3$. Quenching of the PL intensity shows a decreased rate of charge carrier recombination, which confirms the enhanced photogenerated charge carrier separation through the heterojunction. The photocatalytic stability of the prepared materials was confirmed by recycling experiments. After performing the experiment for four cycles (16 h) with the same sample, we could not observe any significant change in photocatalytic hydrogen evolution, which indicates $CuCo_2S_4/g$-$C_3N_4/In_2S_3$ as stable photocatalysts. We believe that this work will be helpful to develop new hetero-structured photocatalysts for enhanced photocatalytic hydrogen evolution.

# Experimental section

### Synthesis of $g$-$C_3N_4$ nanosheets

Typically, $g$-$C_3N_4$ was synthesised by a simple calcination method in a muffle furnace with a fixed rate of temperature increase.[34] 5 g of melamine was putted into a crucible boat and then placed into the muffle furnace and heated at 550 °C for 5 hours with a ramping rate of 3 °C $min^{-1}$. After completing the process, the sample was allowed to cool gently, and then a yellow coloured material was collected and ground well to form a fine powder. 1 g of $g$-$C_3N_4$ powder was dispersed in 100 mL isopropanol and sonicated for 2 h to form $g$-$C_3N_4$ nanosheets by exfoliation of bulk $g$-$C_3N_4$. The dispersion was allowed to stand so that larger particles will settle down. After that, the supernatant was centrifuged and then dried at 60 °C overnight to obtain $g$-$C_3N_4$ nanosheets, which were collected and stored for further use.

### Synthesis of $CuCo_2S_4$ nanoparticles

$CuCo_2S_4$ nanoparticles were synthesised by the hot inject method the same as mentioned in ref. 36 with slight modification. For the synthesis of $CuCo_2S_4$, 1 mmol of copper acetate ($Cu(OAc)_2$), 2 mmol of cobalt acetate ($CoAc_2$) and 3.5 mmol of TOPO were dissolved in 15 mL of oleylamine with continuous stirring in a three necked round bottom flask. The solution was degassed for $\frac{1}{2}$ hour followed by heating at 150 °C for 1 hour under nitrogen gas flow to avoid moisture and confirm an anaerobic reaction medium. After that the temperature of the solution was increased to 250 °C under nitrogen flow. At this temperature, when the colour of the solution changed from dark blue to pale blue, 2.0 mL of 1-DDT was rapidly injected

into the hot solution, which resulted in an immediate colour change of the solution from blue to dark black and the reaction was allowed to run for 1 h at this temperature. Finally, the reaction system was cooled down to room temperature, washed with ethanol to remove excess TOPO and oleylamine, and dried at 60 °C under vacuum. The black coloured sample was dispersed in toluene to remove residual organic components.

### Fabrication of $CuCo_2S_4$/g-$C_3N_4$, $CuCo_2S_4$/$In_2S_3$ and $CuCo_2S_4$/ g-$C_3N_4$/$In_2S_3$ heterostructures

The first step of synthesis of heterostructures is like the synthesis of $CuCo_2S_4$ nanoparticles. A suitable amount of g-$C_3N_4$, copper acetate, cobalt acetate and TOPO was added in 15 mL oleylamine in three necked round bottom flasks. Then the solution was degassed, heated at 150 °C for 1 h under a nitrogen atmosphere and finally the reaction temperature was increased to 250 °C and the reaction was allowed to run for 1 h. After completion of the reaction, the system was cooled to room temperature. Next, the obtained reaction mixture consisting of $CuCo_2S_4$/g-$C_3N_4$ was heated again to 160 °C and a specified amount of $InCl_3$ dissolved in oleylamine was rapidly injected into the solution and the reaction temperature was increased to 250 °C.

## Results and discussion

### X-ray diffraction (XRD) analysis

The crystalline structure and the phase of the as-prepared photocatalysts $CuCo_2S_4$, g-$C_3N_4$, $In_2S_3$, $CuCo_2S_4$/g-$C_3N_4$ and $CuCo_2S_4$/g-$C_3N_4$/$In_2S_3$ were determined by powder XRD analysis (Fig. 1a). Pristine $CuCo_2S_4$ reveals diffraction peaks at 16.13°, 26.59°, 31.27°, 37.97°, 46.99°, 49.99° and 54.79° corresponding to (111), (002), (113), (004), (224), (115) and (044), respectively, matching well with the standard diffraction data (JCPDS No.: 42-1450).[37] The formation of $CuCo_2S_4$/g-$C_3N_4$ and $CuCo_2S_4$/ g-$C_3N_4$/$In_2S_3$ shows the same diffraction pattern similar to pure $CuCo_2S_4$, which indicates that the formation of a heterojunction has no impact on the crystal structure of $CuCo_2S_4$. The broader peaks observed at 14° and 20.7° can be assigned to the (100) and (002) planes of g-$C_3N_4$.[34] The observed peak of g-$C_3N_4$ is very weak in the composites due to the less content and ultrathin sheets of g-$C_3N_4$. Furthermore, the diffraction patterns of $In_2S_3$ also appear clearly in the $CuCo_2S_4$/g-$C_3N_4$/$In_2S_3$ composite. The characteristic peaks related to pristine $In_2S_3$ are matched to previous reports.[38] It is demonstrated that g-$C_3N_4$ and $In_2S_3$ particles coexist in the $CuCo_2S_4$-derived as-synthesized photocatalysts.

### Fourier transform infrared (FTIR) spectroscopy

The composition of $CuCo_2S_4$/g-$C_3N_4$/$In_2S_3$ and functional groups of g-$C_3N_4$ in the hybrid photocatalyst were further examined by FTIR analysis. Fig. S1 (ESI†) exhibits FTIR spectra of g-$C_3N_4$, $CuCo_2S_4$/g-$C_3N_4$ and $CuCo_2S_4$/g-$C_3N_4$/$In_2S_3$. The peak that appeared at 802 cm$^{-1}$ is attributed to the $S$-triazine ring mode. The peaks that appeared at 1243, 1323, and 1411 cm$^{-1}$
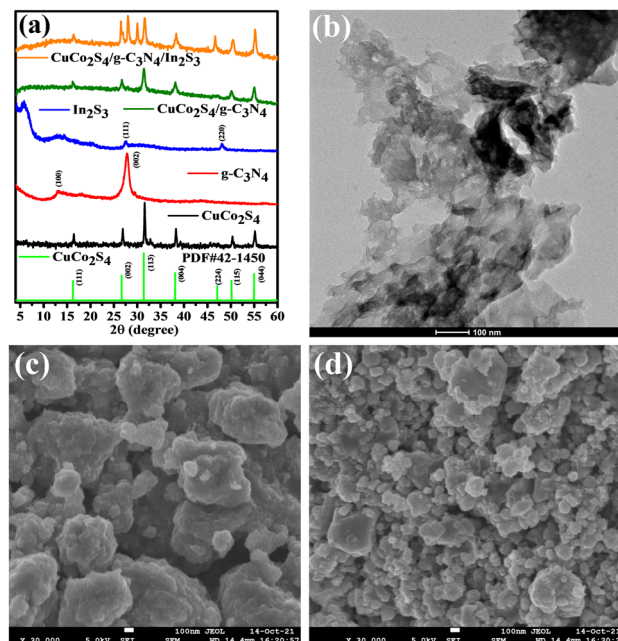


**Fig. 1** (a) X-ray diffraction pattern of the as-prepared catalysts; FESEM images (b) g-$C_3N_4$; (c) $CuCo_2S_4$, and (d) $CuCo_2S_4$/g-$C_3N_4$/$In_2S_3$.

are due to aromatic C–N stretching, whereas the peak that appeared at 1636 cm$^{-1}$ is related to the C=N stretching mode. The O–H and N–H stretching vibration is observed at 3072 and 3180 cm$^{-1}$, respectively. Furthermore, all the characteristic absorption peaks of g-$C_3N_4$ were observed in $CuCo_2S_4$/g-$C_3N_4$ and $CuCo_2S_4$/g-$C_3N_4$/$In_2S_3$, which indicates retention of the structural properties of g-$C_3N_4$ during heterostructure formation.

### Structural morphology studies

The morphology and microstructure of the as-prepared materials were investigated by FE-SEM and TEM analyses. The FESEM image of the pure g-$C_3N_4$ sample displayed an aggregated morphology with a large size and lamellar structure (Fig. 1b). It possessed a layered structure and it is present in the form of a thin sheet with irregular morphology. Fig. 1c shows the aggregated structure of $CuCo_2S_4$ in the FE-SEM image with different particle sizes and stacked in layers. The degree of aggregation of particles is reduced in the $CuCo_2S_4$/g-$C_3N_4$/$In_2S_3$ heterostructure (Fig. 1d). This may happen due to dispersion of $CuCo_2S_4$ particles on a large surface area and interaction with g-$C_3N_4$. This is beneficial because smaller particles increase the specific surface area as well as catalytic active sites for reactants. The size of the synthesised material particles is about that of quantum dots, so it was not possible to determine the exact size of the particles by FE-SEM analysis. Furthermore, the presence of constituent elements was confirmed by EDS analysis. Fig. S2 (ESI†) shows the presence of all the major elements (Cu, Co, In, S, C and N) in $CuCo_2S_4$/g-$C_3N_4$/$In_2S_3$.

Furthermore, the TEM images of $CuCo_2S_4$ (Fig. 2a–c) show discrete particle size ranges from 10–20 nm. The high-resolution TEM image (Fig. 2d) reveals the lattice fringes with an interlayer spacing of $d$ = 0.28 nm which is related to the (113)
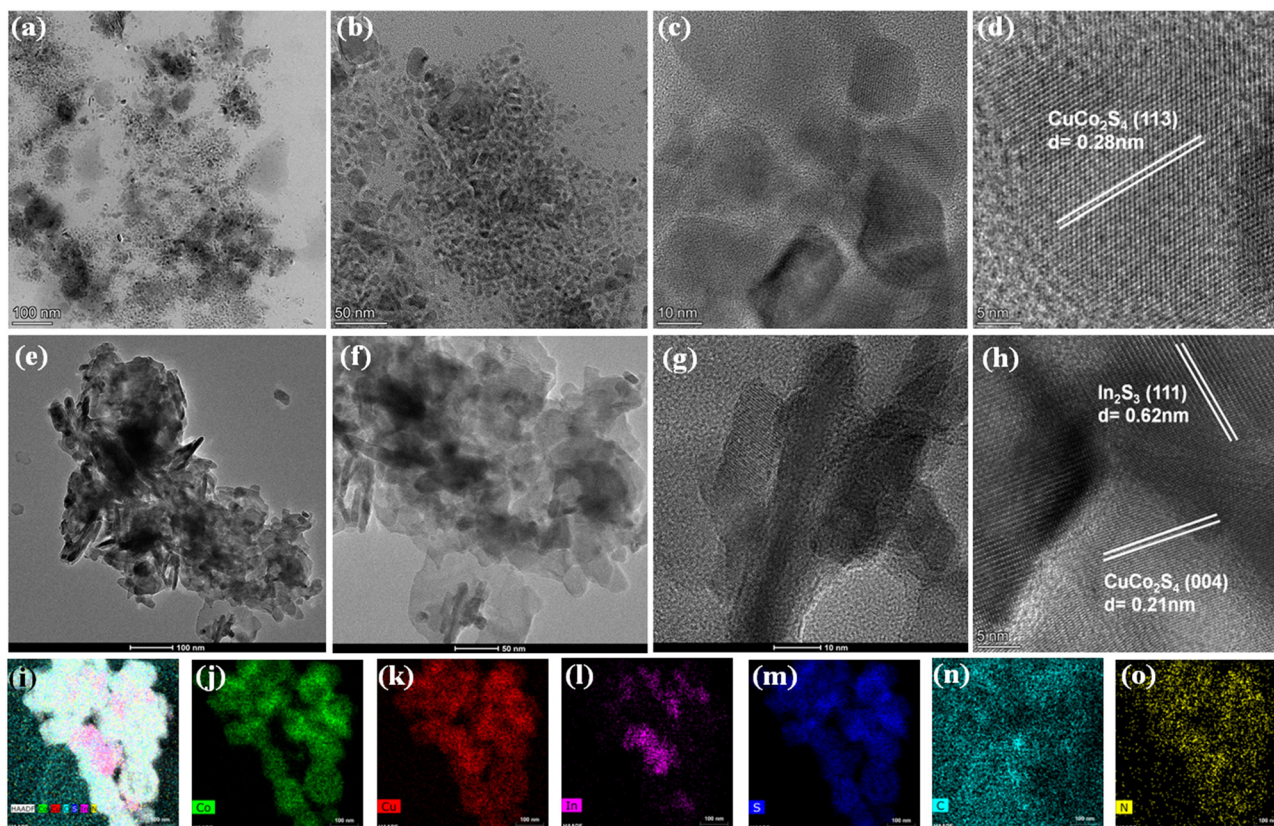
Fig. 2 TEM images of (a) and (b) $CuCo_2S_4$, and (e) and (f) $CuCo_2S_4$/g-$C_3N_4$/$In_2S_3$; HR-TEM images of (c) and (d) $CuCo_2S_4$, and (g) and (h) $CuCo_2S_4$/g-$C_3N_4$/$In_2S_3$; (i)–(o) elemental mapping of Co, Cu, In, S, C, N for $CuCo_2S_4$/g-$C_3N_4$/$In_2S_3$.

plane.[39] The TEM images of $CuCo_2S_4$/g-$C_3N_4$/$In_2S_3$ shown in Fig. 2e–g illustrate that the $CuCo_2S_4$ and $In_2S_3$ nanoparticles were dispersed on the g-$C_3N_4$ sheet. Fig. 2(f and g) shows the presence of all three components, and $CuCo_2S_4$ shows a roughly square shaped morphology while $In_2S_3$ has a rod-like appearance in composite, which are dispersed on the g-$C_3N_4$ nanosheets while hexagonal sheet like appearance was observed in TEM analysis of $In_2S_3$ as single component. The formation of a heterostructure shows the agglomeration of particles, which may be due to particles being covered by g-$C_3N_4$ nanosheets. The HR-TEM image (Fig. 2h) reveals two different interlayer spacings of 0.62 nm and 0.21 nm, which are attributed to the (111) plane of $In_2S_3$ and (004) plane of $CuCo_2S_4$, respectively. The formation of a heterojunction creates an additional electron transfer pathway, which facilitates suppression of the recombination of photo-induced electron hole pairs. The microstructural distribution of elements in the composite was confirmed by elemental mapping. Fig. 2(i–o) shows the uniform distribution of all constituent elements Cu, Co, In, S, C and N in $CuCo_2S_4$/g-$C_3N_4$/$In_2S_3$. Furthermore, the TEM analysis of g-$C_3N_4$ (Fig. S3a and b, ESI†), $In_2S_3$ (Fig. S3c and d, ESI†) and $CuCo_2S_4$/g-$C_3N_4$ (Fig. S3e and f, ESI†) was also carried out for comparative study. TEM analysis of $CuCo_2S_4$/g-$C_3N_4$/$In_2S_3$ after photocatalytic reaction (Fig. S4, ESI†) shows the presence of all the components and constituent elements, which indicates the stability of $CuCo_2S_4$/g-$C_3N_4$/$In_2S_3$ in the photocatalytic reaction.

## X-ray photoelectron spectroscopy (XPS) studies

The XPS analysis was performed to analyse the chemical composition of the $CuCo_2S_4$/g-$C_3N_4$/$In_2S_3$ composite and chemicals state of the elements. Fig. S5 (ESI†) is the XPS survey spectrum of $CuCo_2S_4$/g-$C_3N_4$/$In_2S_3$ composed of N, C, Cu, Co, In, and S elements. In addition, Fig. 3a exhibits the C 1S spectra of the composite. The C 1S spectra can be observed at 280 eV. Due to the overlap, the peaks of C 1s cannot be deconvoluted. The peak which appeared at 398 eV is related to the sp² hybridised carbon atom bonded to the N atom in the aromatic rings (–N–C=N–) of g-$C_3N_4$, which represents the main source of carbon in g-$C_3N_4$.[40] The N 1S spectrum shows an asymmetric feature, and it can be fitted to three peaks at 397, 399 and 403.6 eV (Fig. 3b), which indicates more than one chemical environment of nitrogen. The peak that appeared at 397 eV can be assigned to sp² nitrogen bonded to carbon in a triazine ring, and the peaks at 399 eV and 403.6 eV originate due to the tertiary nitrogen N–(C)₃ of the aromatic ring and amino nitrogen (–NH₂), respectively. Fig. 3c illustrates the photoelectron spectra of Cu 2p. The peaks that appeared at 932.1 and 950 eV correspond to spin–orbit coupling of Cu $2p_{3/2}$ and Cu $2p_{1/2}$.[17,23] The separation between the two peaks is 19.9 eV, which indicates the +1-valence state of copper. The XPS of Co 2p shows four peaks; the two peaks that appeared at 774.1 and 789 eV are attributed to $Co^{3+}$ $2p_{3/2}$ and $Co^{3+}$ $p_{1/2}$, while the peaks at binding energy

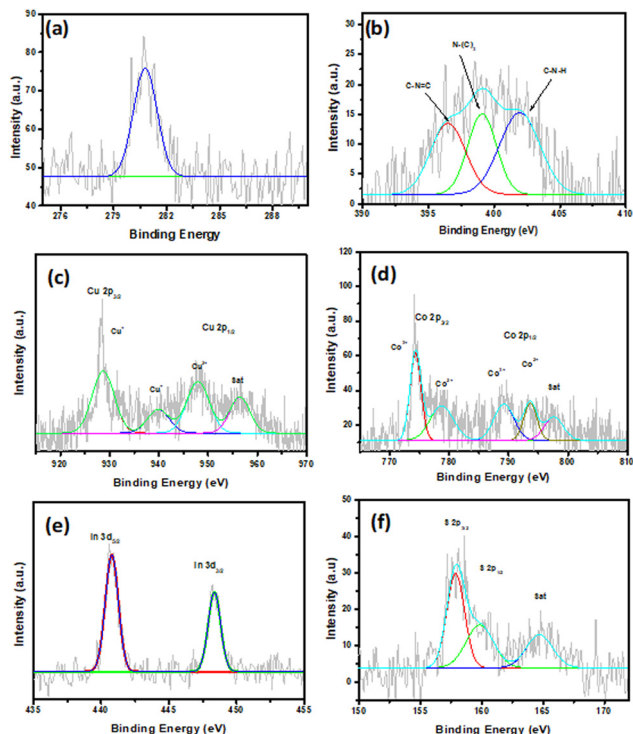**Fig. 3** XPS spectra of the $CuCo_2S_4/g\text{-}C_3N_4/In_2S_3$ composite: (a) C 1s, (b) N 1s, (c) Cu 2p, (d) Co 2p, (e) In 3d, and (f) S 2p.
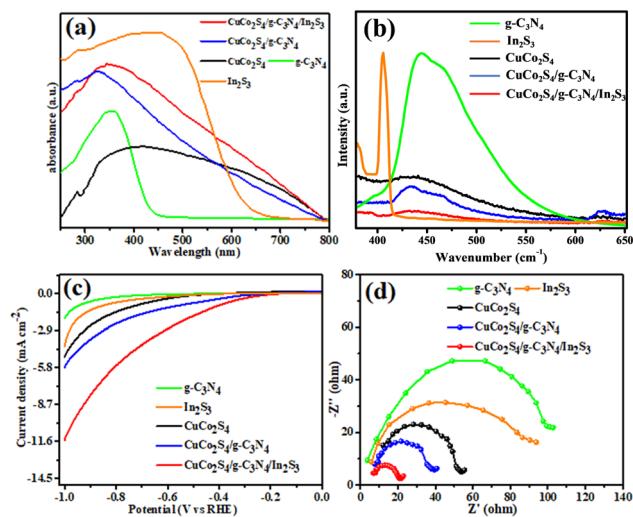


**Fig. 4** (a) UV-Vis DRS profiles, (b) photoluminescence (PL) spectra, (c) linear sweep voltammetry (LSV) curves and (b) EIS Nyquist plots of the as-prepared materials.

778.8 and 793 eV are related to $Co^{2+}$ $2p_{3/2}$ and $Co^{2+}$ $2p_{1/2}$, respectively (Fig. 3d).[17,19,41] This result indicates multiple states of cobalt in $CuCo_2S_4$. The spectra of $In_2S_3$ include two peaks that appeared at 440.78 and 448.3 eV, which are assigned to $3d_{5/2}$ and $3d_{3/2}$ of $In^{3+}$ of $In_2S_3$ (Fig. 3e).[42] Furthermore, the S 2p spectrum shows two peaks at 161.3 and 162.4 eV, which could be ascribed to S $2p_{1/2}$ and S $2p_{3/2}$, respectively (Fig. 3f).[15,17,20] The peak that appeared at 187 eV is related to a satellite peak.

### Ultraviolet diffused reflectance spectroscopy (UV-Vis DRS) studies

The optical behaviour of $CuCo_2S_4$, $g\text{-}C_3N_4$, $In_2S_3$, $CuCo_2S_4/g\text{-}C_3N_4$ and $CuCo_2S_4/g\text{-}C_3N_4/In_2S_3$ was explored by UV-Vis DRS absorption analysis. Fig. 4a exhibits the absorption spectra of the prepared materials. $CuCo_2S_4$ shows wide absorption in the visible region and intense absorption at 400 nm, whereas pure $g\text{-}C_3N_4$ has an absorption edge at about 460 nm. The formation of a composite enhances light harvesting in the ultraviolet to visible region. Moreover, the maximum light absorption peak of the composite shifted to a lower wavelength; however, the overall absorption is red shifted, which is confirmed by comparison of the band gap of pristine $CuCo_2S_4$ and the composite materials. The red shift and enhanced absorption of the composite indicates the trapping of more light to generate a greater number of photo-generated electron–hole pairs due to the $In_2S_3$ showing the strongest visible light absorption. The increased light harvesting and red shift of $CuCo_2S_4/g\text{-}C_3N_4$ and $CuCo_2S_4/g\text{-}C_3N_4/In_2S_3$ could be due to the formation a

heterostructure, which significantly affects the band gap and electronic properties of the composite.

We further estimated the optical band gap ($E_g$) of the prepared samples by Tauc plot by using the following equation:

$$E_g = \frac{1240}{\lambda} \tag{3}$$

where $\lambda$ is the wavelength of the absorption edge. The estimated bandgap of $CuCo_2S_2$, $CuCo_2S_4/g\text{-}C_3N_4$ and $CuCo_2S_4/g\text{-}C_3N_4/In_2S_3$ was 1.66, 2.57 and 2.22 eV, respectively (Fig. S6, ESI†). The optical band gap of $CuCo_2S_4$ was found like in our previous report.[17]

### Photoluminescence (PL) spectroscopy

The photoluminescence studies were carried out to investigate the separation/migration efficacy of photo-induced charge carriers in the composite materials. As shown in Fig. 4b, $CuCo_2S_4$ shows an intense emission peak at 430 nm with excitation of 350 nm wavelength. It is generally known that the PL intensity stems from the recombination of photo-induced charge carriers. $CuCo_2S_4/g\text{-}C_3N_4/In_2S_3$ exhibits the maximum decrease of the PL intensity compared to $g\text{-}C_3N_4$, $In_2S_3$, $CuCo_2S_4$ and $CuCo_2S_4/g\text{-}C_3N_4$, indicating the rapid separation of photo-induced charge carriers, which can be ascribed to the 2-D sheet-like structure and excellent conductivity of $g\text{-}C_3N_4$, which can delocalize photo-induced electrons and holes. $In_2S_3$ further suppresses the recombination of charge carriers by creating an additional pathway for electron hole separation.

### Electrochemical studies

To explore the role of heterostructures $CuCo_2S_4/g\text{-}C_3N_4$ and $CuCo_2S_4/g\text{-}C_3N_4/In_2S_4$ for improving photo-generated charge carrier separation, linear sweep voltammetry (LSV) of different samples was carried out. Fig. 4c illustrates the LSV graph of $g\text{-}C_3N_4$, $In_2S_3$, $CuCo_2S_4$, $CuCo_2S_4/g\text{-}C_3N_4$ and $CuCo_2S_4/g\text{-}C_3N_4/In_2S_3$. This result

indicates that the formation of a heterojunction accelerates the photo-induced electron and hole separation. The 2D ultrathin sheet of g-C$_3$N$_4$ stabilizes the photo-induced electrons from CuCo$_2$S$_4$ and transfers them to In$_2$S$_3$, which increases the pathway of electron transfer, suppressing recombination of electrons and holes. The improved charge separation efficiency of the heterostructured photocatalyst was further confirmed by electrochemical impedance spectroscopy (EIS) analysis. EIS is an important tool to examine the charge transfer resistance and super capacitive efficiency. It consists of a semicircle at higher frequency and a line in the low frequency region. The smallest semicircle radius of CuCo$_2$S$_4$/g-C$_3$N$_4$/In$_2$S$_3$ shows that it exhibits the lowest resistance of interfacial charge transfer, which indicates higher electrical conductivity of the CuCo$_2$S$_4$/g-C$_3$N$_4$/In$_2$S$_3$ composite. Fig. 4d clearly illustrates the increased charge transfer in the order of g-C$_3$N$_4$ < In$_2$S$_3$ < CuCo$_2$S$_4$ < CuCo$_2$S$_4$/g-C$_3$N$_4$ < CuCo$_2$S$_4$/g-C$_3$N$_4$/In$_2$S$_4$. The low activity of g-C$_3$N$_4$, In$_2$S$_3$ and CuCo$_2$S$_4$ is due to the high resistance for charge transfer, while the low resistance of charge transfer of CuCo$_2$S$_4$/g-C$_3$N$_4$/In$_2$S$_3$ results in excellent electrical conductivity, indicating the best photocatalyst among the others for energy conversion systems.

### Photocatalytic hydrogen evolution activity

The photocatalytic hydrogen evolution over different photocatalysts CuCo$_2$S$_4$, g-C$_3$N$_3$, In$_2$S$_3$, CuCo$_2$S$_4$/g-C$_3$N$_4$, CuCo$_2$S$_4$/In$_2$S$_3$ and CuCo$_2$S$_4$/g-C$_3$N$_4$/In$_2$S$_3$ was evaluated in aqueous Na$_2$S and Na$_2$SO$_3$ solution and under a 300 W Xe-lamp equipped with a cut-off filter ($\lambda \geq 420$ nm; ESI,† experimental section). The Na$_2$S and Na$_2$SO$_3$ were employed as a sacrificial electron donor. A controlled experiment indicated that in the absence of light or catalyst no hydrogen was detected, which confirms the

dependence of water splitting on light and the photocatalyst. Table S1 (ESI†) shows the hydrogen evolution rate over different photocatalysts performed under visible light irradiation. Pure g-C$_3$N$_4$, In$_2$S$_3$ and CuCo$_2$S$_4$ show extremely low hydrogen evolution efficiency. Low charge separation efficiency and inadequate surface-active sites of single photocatalysts speed up charge carrier recombination, which greatly reduces the hydrogen evolution efficiency. The fabrication of the heterojunction significantly increases the hydrogen evolution rate, where the H$_2$ evolution rate was found to be CuCo$_2$S$_4$ ($\sim$1.32 mmol g$^{-1}$ h$^{-1}$), CuCo$_2$S$_4$/In$_2$S$_3$ ($\sim$3.92 mmol g$^{-1}$ h$^{-1}$), CuCo$_2$S$_4$/g-C$_3$N$_4$ ($\sim$5.19 mmol g$^{-1}$ h$^{-1}$) and CuCo$_2$S$_4$/g-C$_3$N$_4$/In$_3$S$_3$ ($\sim$11.66 mmol g$^{-1}$ h$^{-1}$; Fig. 5a). The formation of CuCo$_2$S$_4$/g-C$_3$N$_4$/In$_3$S$_3$ further improves the catalytic efficiency. It is investigated that the CuCo$_2$S$_4$/g-C$_3$N$_4$/In$_2$S$_3$ photocatalyst with 4 wt% g-C$_3$N$_4$ and 5 wt% In$_2$S$_3$ to CuCo$_2$S$_4$ shows the highest catalytic hydrogen evolution activity, which is around nine times higher than that of CuCo$_2$S$_4$. Coupling of g-C$_3$N$_4$ and In$_2$S$_3$ synergistically improves the charge separation efficiency. Further increasing the content of g-C$_3$N$_4$ and In$_2$S$_3$ decreases the catalytic activity. This effect may arise due to the light shielding and less availability of active sites caused by excess g-C$_3$N$_4$ and In$_2$S$_3$. Table S1 (ESI†) illustrates the rate of hydrogen evolution efficiency and apparent quantum yield (AQY) of the as-prepared photocatalyst in the present work. To better understand the advantages of our noble photocatalyst, the recently reported results are summarized in Table S2 (ESI†). Furthermore, the stability of the photocatalysts and retention of the catalytic efficiency were confirmed by a cycled hydrogen evolution experiment with the same catalyst. Fig. 5b shows the results of the recycled hydrogen evolution experiment. No
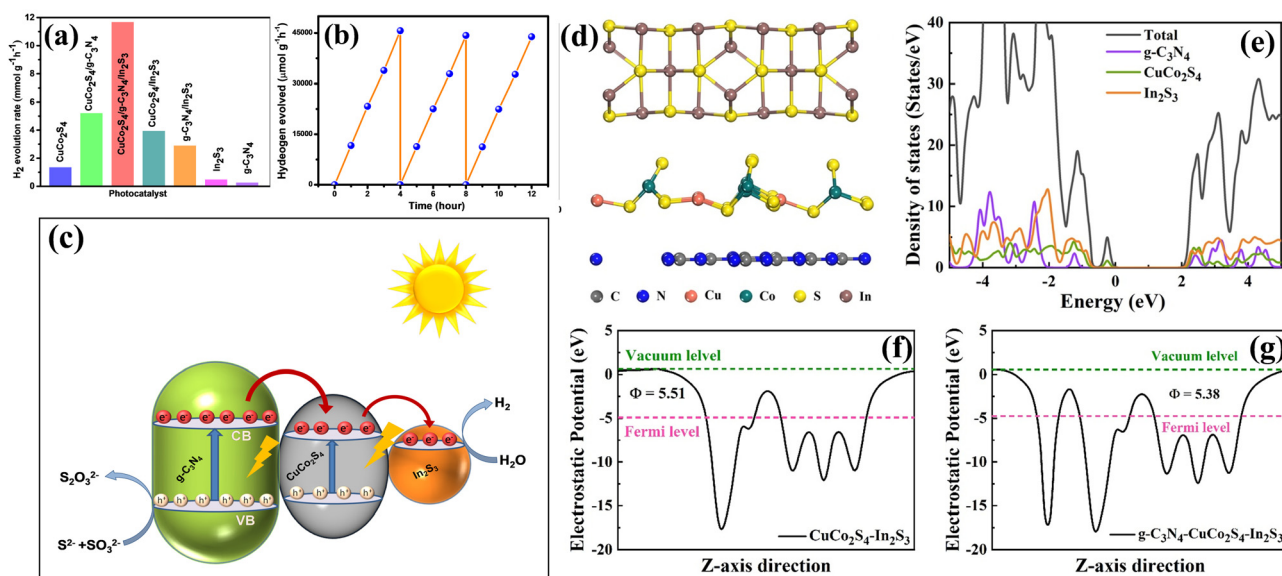


**Fig. 5** (a) Histogram of the photocatalytic H$_2$ production rate of the as-synthesized photocatalysts for 4 h visible light irradiation, (b) photo stability recycling experiment of CuCo$_2$S$_4$/g-C$_3$N$_4$/In$_2$S$_3$, and (c) schematic presentation of the mechanism of photocatalytic hydrogen evolution on the CuCo$_2$S$_4$/g-C$_3$N$_4$/In$_2$S$_3$ photocatalyst; (d) optimized geometry of the CuCo$_2$S$_4$/g-C$_3$N$_4$/In$_2$S$_3$ ternary heterostructure and (e) corresponding partial density of states; the calculated electrostatic potentials of (f) CuCo$_2$S$_4$/In$_2$S$_3$ and (g) CuCo$_2$S$_4$/g-C$_3$N$_4$/In$_2$S$_3$. Here, the green and pink dashed lines denote the vacuum level and the Fermi level, respectively.

significant change in hydrogen evolution activity was observed after irradiation for 20 hours. Furthermore, the TEM analyses of the $CuCo_2S_4$/g-$C_3N_4$/$In_2S_3$ photocatalyst after the HER also presented the stability of the catalyst. The TEM investigations also confirmed that the morphology of the $CuCo_2S_4$/g-$C_3N_4$/$In_2S_3$ photocatalyst was preserved after the HER (Fig. S4, ESI†). This is in agreement with before the HER experiment, which indicates the higher stability of the $CuCo_2S_4$/g-$C_3N_4$/$In_2S_3$ photocatalyst.

### Mechanism of photocatalytic reaction

The composite $CuCo_2S_4$/g-$C_3N_4$/$In_2S_3$ material, consisting of $CuCo_2S_4$ supported on g-$C_3N_4$ nanosheets with $In_2S_3$ as a co-catalyst, exhibits remarkable photocatalytic activity for hydrogen evolution. It is obvious that the photocatalytic activity of the material depends on the light absorbance, surface properties and separation of photo-induced electron hole pairs. Under visible light irradiation, the g-$C_3N_4$ nanosheets absorb photons and generate electron–hole pairs. The photogenerated electrons are transferred to the conduction band (CB) of $CuCo_2S_4$ because of the more negative conduction band of g-$C_3N_4$ than $CuCo_2S_4$, while the holes remain in the valence band (VB) of g-$C_3N_4$ (Fig. 5c). Meanwhile, the $In_2S_3$ co-catalyst plays a crucial role in the $H_2$ production process. It provides active sites for reaction and the heterojunction facilitates the rapid transfer of photogenerated electrons from $CuCo_2S_4$ to the $In_2S_3$ surface minimizing charge carrier recombination and enhancing the photocatalytic performance. The photogenerated electrons accumulated on the $CuCo_2S_4$/g-$C_3N_4$/$In_2S_3$ reduce adsorbed water molecules and $H_2$ evolution takes place. The photogenerated holes were stabilised by sacrificial electron donors $S^{2-}$/$SO_3^{2-}$. The formation of a heterojunction facilitates the transfer of electrons to a great extent, which was confirmed to reduce the arc radius of the composite in the impedance spectra as compared to the single component. The smallest radius was observed for $CuCo_2S_4$/g-$C_3N_4$/$In_2S_3$, indicating the highest rate of charge transfer amongst all the materials. The reduction reaction occurs at the $In_2S_3$ co-catalyst sites, facilitated by the presence of active surface sites. Hence, the dramatically improved activity of $CuCo_2S_4$/g-$C_3N_4$/$In_2S_3$ for hydrogen evolution can be explained by interfacial contact and synergistic interaction between g-$C_3N_4$, $CuCo_2S_4$ and $In_2S_3$, which facilitates the transfer of electrons by creating an electron transfer channel (g-$C_3N_4$/$CuCo_2S_4$ and $CuCo_2S_4$/$In_2S_3$). The unique structural and compositional characteristics of the $CuCo_2S_4$/g-$C_3N_4$/$In_2S_3$ composite are also attributed to suppressed charge recombination, and improved photocatalytic efficiency.

### Theoretical study

We further performed density functional theory (DFT) calculations to understand the visible-light response of $In_2S_3$ on the $CuCo_2S_4$/g-$C_3N_4$ based heterostructure. The optimized geometry of the $CuCo_2S_4$/g-$C_3N_4$/$In_2S_3$ ternary configuration is shown in Fig. 5d. The geometric changes due to the $CuCo_2S_4$/$In_2S_3$ contribution over g-$C_3N_4$ can be analysed by understanding the electronic properties. The band gap of g-$C_3N_4$ is found to be

2.64 eV, which is significantly larger than the minimum band gap required for photocatalytic water splitting.[43] The g-$C_3N_4$/$CuCo_2S_4$ heterostructure has a smaller band gap (2.26 eV) in comparison to its isolated counterparts, providing an advantage for absorbing visible light. The partial density of states of the $CuCo_2S_4$/g-$C_3N_4$/$In_2S_3$ ternary heterostructure is shown in Fig. 5e. Clearly, the conduction band energy position of the g-$C_3N_4$/$CuCo_2S_4$ heterostructure is modified by the introduction of $In_2S_3$, resulting in a shift to a lower position and thus reducing the band gap to 2.03 eV. Therefore, the PDOS of the $CuCo_2S_4$/g-$C_3N_4$/$In_2S_3$ ternary heterostructure demonstrates that the conduction band minimum is constructed by $In_2S_3$, while $CuSo_2S_4$ dominates the valence band maximum. In addition, we computed the work function ($\Phi$), which refers to the energy required for exciting the electrons from the Fermi level to the vacuum level, representing the minimum energy needed for this process to occur.[19] The work functions of g-$C_3N_4$ and $CuCo_2S_4$ are found to be 5.12 and 5.43 eV, respectively. The lowest $\Phi$ value of g-$C_3N_4$ will cause electrons to flow from the corresponding layer to $CuCo_2S_4$ in the g-$C_3N_4$ based heterostructure. The $\Phi$ values of the $CuCo_2S_4$/$In_2S_3$ and $CuCo_2S_4$/g-$C_3N_4$/$In_2S_3$ configurations are 5.51 and 5.38 eV (Fig. 5f and g), which indicates that the latter have a lower work function when compared with the former. Since the Fermi energy level of g-$C_3N_4$ is greater than that of $CuCo_2S_4$ and $In_2S_3$, the photogenerated electrons will flow from g-$C_3N_4$ to $CuCo_2S_4$/$In_2S_3$ until they reach the same Fermi level. This will enable the electrons of the $CuCo_2S_4$/g-$C_3N_4$/$In_2S_3$ ternary heterostructure to transfer onto the surface and facilitate the redox reaction. Moreover, the observed behaviour will improve the interfacial contact, reducing the size of the electron depletion layers and enhancing the built-in electric field on their catalyst interfaces.

## Conclusion

In view of the unanticipated high surface to volume ratio, small distance for photogenerated charge to travel to reach surface active sites and specific properties of mono-dispersed quantum dots and excellent charge separation efficiency of heterostructured composites, we have designed $CuCo_2S_4$/g-$C_3N_4$/$In_2S_3$ hybrid photocatalysts by the hot injection method. The optimized $CuCo_2S_4$/g-$C_3N_4$/$In_2S_3$ photocatalyst depicts hydrogen evolution activity of 11.66 mmol $g^{-1}$ $h^{-1}$, which is nine times higher than that of $CuCo_2S_4$. The increased activity of the $CuCo_2S_4$/g-$C_3N_4$/$In_2S_3$ photocatalyst is caused by the improved light harvesting, and excellent charge separation efficiency of the $CuCo_2S_4$/g-$C_3N_4$/$In_2S_3$ hybrid photocatalyst. Increased absorption of light generates a greater number of photo-induced electrons for the reduction reaction and improved charge separation efficiency diminishes the rate of electron and hole recombination. Combining these two findings improves the efficiency of $CuCo_2S_4$/g-$C_3N_4$/$In_2S_3$ for hydrogen evolution. A decreased rate of charge carrier recombination is also confirmed by quenching of the photoluminescence intensity of $CuCo_2S_4$/g-$C_3N_4$/$In_2S_4$ compared to $CuCo_2S_4$ and g-$C_3N_4$.

We believe that this work will be useful for the design of efficient photocatalysts for solar energy conversion to hydrogen fuel. This research, in our opinion, will be useful for designing efficient photocatalysts for the utilization of solar energy to $H_2$ energy.

## Conflicts of interest

There are no conflicts to declare.

## Acknowledgements

## Notes and references

1 K. Takanabe, *ACS Catal.*, 2017, **7**, 8006–8022.
2 M. G. Walter, E. L. Warren, J. R. McKone, S. W. Boettcher, Q. Mi, E. A. Santori and N. S. Lewis, *Chem. Rev.*, 2010, **110**, 6446–6473.
3 S. Chandrasekaran, L. Yao, L. Deng, C. Bowen, Y. Zhang, S. Chen, Z. Lin, F. Peng and P. Zhang, *Chem. Soc. Rev.*, 2019, **48**, 4178–4280.
4 S. Protti, A. Albini and N. Serpone, *Phys. Chem. Chem. Phys.*, 2014, **16**, 19790–19827.
5 O. Stroyuk, A. Raevskaya and N. Gaponik, *Chem. Soc. Rev.*, 2018, **47**, 5354–5422.
6 Y. Wang, H. Suzuki, J. Xie, O. Tomita, D. J. Martin, M. Higashi, D. Kong, R. Abe and J. Tang, *Chem. Rev.*, 2018, **118**, 5201–5241.
7 X. Zou and Y. Zhang, *Chem. Soc. Rev.*, 2015, **44**, 5148–5180.
8 S. Gonuguntla, S. Sk, A. Tripathi, R. Thapa, G. Jonnalagadda, C. Nayak, D. Bhattacharyya, S. N. Jha, A. V. Sesha Sainath, V. Perupogu and U. Pal, *Commun. Chem.*, 2022, **5**, 165.
9 T. Di, Q. Xu, W. Ho, H. Tang, Q. Xiang and J. Yu, *ChemCatChem*, 2019, **11**, 1394–1411.
10 K. Chang, X. Hai and J. Ye, *Adv. Energy Mater.*, 2016, **6**, 1502555.
11 A. Gautam, S. Sk and U. Pal, *Phys. Chem. Chem. Phys.*, 2022, **24**, 20638–20673.
12 S. Sk, R. Madhu, D. S. Gavali, V. Bhasin, R. Thapa, S. N. Jha, D. Bhattacharyya, S. Kundu and U. Pal, *J. Mater. Chem. A*, 2023, **11**, 10309–10318.
13 A. Fujishima and K. Honda, *Nature*, 1972, **238**, 37–38.
14 X. Chen, S. Shen, L. Guo and S. S. Mao, *Chem. Rev.*, 2010, **110**, 6503–6570.
15 A. Tiwari, A. Gautam, S. Sk, D. S. Gavali, R. Thapa and U. Pal, *J. Phys. Chem. C*, 2021, **125**, 11950–11962.
16 Y.-L. Lee, C.-F. Chi and S.-Y. Liau, *Chem. Mater.*, 2010, **22**, 922–927.
17 A. Gautam, S. Sk, B. M. Abraham, A. Dutta, P. Sen and U. Pal, *Int. J. Hydrogen Energy*, 2022, **47**, 23632–23643.
18 S. Guo, H. Luo, X. Duan, B. Wei and X. Zhang, *Nanomaterials*, 2022, **12**, 1761.
19 S. Sk, C. S. Vennapoosa, A. Tiwari, B. M. Abraham, M. Ahmadipour and U. Pal, *Int. J. Hydrogen Energy*, 2022, **47**, 33955–33965.
20 A. Gautam, S. Sk, A. Tiwari, B. M. Abraham, V. Perupogu and U. Pal, *Chem. Commun.*, 2021, **57**, 8660–8663.
21 J. Dong, W. Fang, H. Yuan, W. Xia, X. Zeng and W. Shangguan, *ACS Appl. Energy Mater.*, 2022, **5**, 4893–4902.
22 S. Kumar, A. Kumar, V. Navakoteswara Rao, A. Kumar, M. V. Shankar and V. Krishnan, *ACS Appl. Energy Mater.*, 2019, **2**, 5622–5634.
23 S. Sk, A. Tiwari, B. M. Abraham, N. Manwar, V. Perupogu and U. Pal, *Int. J. Hydrogen Energy*, 2021, **46**, 27394–27408.
24 C. S. Vennapoosa, S. Gonuguntla, S. Sk, B. M. Abraham and U. Pal, *ACS Appl. Nano Mater.*, 2022, **5**, 4848–4859.
25 G. Ou, P. Fan, X. Ke, Y. Xu, K. Huang, H. Wei, W. Yu, H. Zhang, M. Zhong, H. Wu and Y. Li, *Nano Res.*, 2018, **11**, 751–761.
26 J. Sakizadeh, J. P. Cline, M. A. Snyder, C. J. Kiely and S. McIntosh, *ACS Appl. Mater. Interfaces*, 2020, **12**, 42773–42780.
27 J. He, B. Li, J. Yu, L. Qiao, S. Li, X. Zu and X. Xiang, *Optic. Mater.*, 2020, **108**, 110231.
28 S. Wang, B. Y. Guan, X. Wang and X. W. D. Lou, *J. Am. Chem. Soc.*, 2018, **140**, 15145–15148.
29 X. Shi, C. Dai, X. Wang, J. Hu, J. Zhang, L. Zheng, L. Mao, H. Zheng and M. Zhu, *Nat. Commun.*, 2022, **13**, 1287.
30 J. Ding, B. Hong, Z. Luo, S. Sun, J. Bao and C. Gao, *J. Phys. Chem. C*, 2014, **118**, 27690–27697.
31 K. Li, S. Zhang, Y. Li, J. Fan and K. Lv, *Chin. J. Catal.*, 2021, **42**, 3–14.
32 J.-H. Zhang, M.-J. Wei, Z.-W. Wei, M. Pan and C.-Y. Su, *ACS Appl. Nano Mater.*, 2020, **3**, 1010–1018.
33 P. Babu, H. Kim, J. Y. Park and B. Naik, *Inorg. Chem.*, 2022, **61**, 1368–1376.
34 S. Gonuguntla, S. Sk, A. Tiwari, H. Mandal, P. N. Lakavath, V. Perupoga and U. Pal, *J. Mater. Sci.: Mater. Electron.*, 2021, **32**, 12191–12207.
35 Q. Zhu, Z. Xu, B. Qiu, M. Xing and J. Zhang, *Small*, 2021, **17**, 2101070.
36 M. Kruszynska, H. Borchert, J. Parisi and J. Kolny-Olesiak, *J. Am. Chem. Soc.*, 2010, **132**, 15976–15986.
37 L. Li, J. Xu, J. Ma, Z. Liu and Y. Li, *J. Colloid Interface Sci.*, 2019, **552**, 17–26.

38 Q. Hu, G. Chen, Y. Wang, J. Jin, M. Hao, J. Li, X. Huang and J. Jiang, *Nanoscale*, 2020, **12**, 12336–12345.

39 Y. Ge, J. Wu, X. Xu, M. Ye and J. Shen, *Int. J. Hydrogen Energy*, 2016, **41**, 19847–19854.

40 X.-H. Jiang, L.-C. Wang, F. Yu, Y.-C. Nie, Q.-J. Xing, X. Liu, Y. Pei, J.-P. Zou and W.-L. Dai, *ACS Sustainable Chem. Eng.*, 2018, **6**, 12695–12705.

41 S. Sk, I. Mondal, A. Mahata, B. M. Abraham, C. Nayak, D. Bhattacharyya, S. N. Jha, R. Ghosh and U. Pal, *ACS Appl. Energy Mater.*, 2022, **5**, 12324–12335.

42 S. B. Kokane, R. Sasikala, D. M. Phase and S. D. Sartale, *J. Mater. Sci.*, 2017, **52**, 7077–7090.

43 T. Bhoyar, D. J. Kim, B. M. Abraham, S. Tonda, N. R. Manwar, D. Vidyasagar and S. S. Umare, *Appl. Catal., B*, 2022, **310**, 121347.